ACS OMEGA

http://pubs.acs.org/journal/acsodf

Article

High-Resolution Femtosecond Laser-Induced Carbon and Ag Hybrid Structure for Bend Sensing

Quan Hong, Weihua Zhu, Sumei Wang,* Lan Jiang, Jiahua He, Jie Zhan, Xin Li, Xiaoming Zhao, and Bingquan Zhao

Cite This: *ACS Omega* 2022, 7, 42256−42263

Read Online

ACCESS | Metrics & More | Article Recommendations | Supporting Information

ABSTRACT: Miniaturized resistance-based portable bending sensors have been widely used for human health monitoring in recent years. Their sensitivities are defined by their resistance variations ($\Delta R/R$), which strongly rely on the conductivity and minimum line width of the sensing unit. Laser-induced carbonization is a fast and simple method to fabricate porous-sensing structures. However, the fabrication resolution of conductive and deformation-sensitive structures is limited by the thermal effect of commonly used laser sources. With the assistance of femtosecond laser temporal shaping, plasma ejection confinement, and silver nitrate doping, the sheet resistance of the sensing structure was improved from 15 to 0.0004 Ω/□. A thin line with a lateral resolution of 6.5 μm is fabricated as the sensing unit. The fFabricated structures are characterized by electron microscopy, Raman spectroscopy, energy-dispersive spectroscopy, X-ray scattering, and time-resolved images. The strain sensor demonstrates a $\Delta R/R$ of 25.8% with a rising edge of 109 ms in the cyclic bending test. The sensor is further applied for detecting human pulse and finger bending.

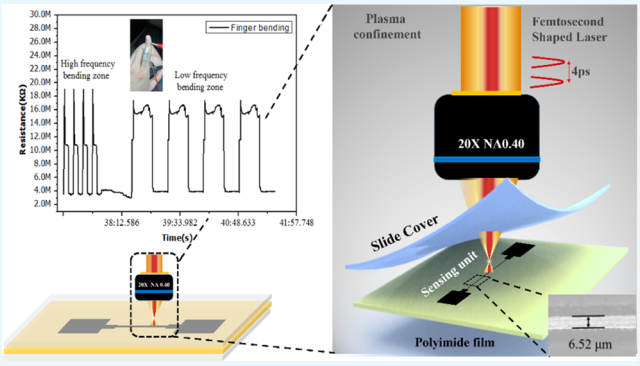

1. INTRODUCTION

Flexible and wearable sensors are very important for monitoring people's health status. Laser-induced graphene (LIG), laser-induced carbonization, or laser-scribed graphene is a facile approach for flexible sensor fabrication with advantages of high porosity, arbitrary patterning, and excellent electric and thermal conductivity.[1−4] Sensors fabricated by LIG have been applied for respiratory and heartbeat monitoring,[5,6] human motion recognition,[7] human disease detection, and control.[8] Also, hybrid structures with nanoparticles have been demonstrated by LIG and applied for chemical[9] or photoelectrochemical sensing.[10,11] Among the various kinds of sensors mentioned above, the sensitivity of the piezoresistive effect-based mechanical sensors is particularly sensitive to the line shape, the conductivity, and the resolution of the fine line.[8,12,13] Yang et al. showed that piezoresistive strain sensors with straight lines yield a higher strain response when compared with those with a serpentine line.[8] Rahimi et al. provided a minimum of 200 μm traces with the highest sensitivity of 0.35 (R/R_o) per degree radius of curvature.[12] Zhang et al. provided the dependence of resistance on phenolic resin—LIG lines and found that the resistance decreased rapidly as the line width increased.[13] Thus, lowering the resistance and improving the resolution of the structures with straight lines can increase the sensitivity of the sensor since the resistance variation ($\Delta R/R$) increases.

It has been reported that a commonly used CO_2 laser for carbonization typically produces 60−300 μm line widths due to beam optics and diffraction limitations.[14−16] To further minimize the line width, pulsed laser sources with a shorter wavelength were applied. Carvalho[17] et al. decreased the penetration depth to 5 μm and a lateral resolution of 50 μm by using a pulsed laser with a wavelength of 355 nm. Stanford[18] et al. presented a formation method of LIG with a lateral resolution of ∼12 μm using a 405 nm pulsed laser. A femtosecond (fs) laser is a better choice to improve the structure resolution since it can control the electron dynamics through temporal or spatial shaping.[19] Miniaturized microsupercapacitors with a submicron resolution of ∼800 nm were fabricated using a temporal-shaped fs laser.[20] However, the insufficient photothermal effect of a laser with a low repetition rate and a short pulse width makes it hard to transfer polyimide (PI) into conductive graphene structures.[18] Metallic nanoparticle doping is an effective way to improve the structure conductivity or introduce novel functions during the LIG

Received: August 8, 2022
Accepted: November 2, 2022
Published: November 11, 2022

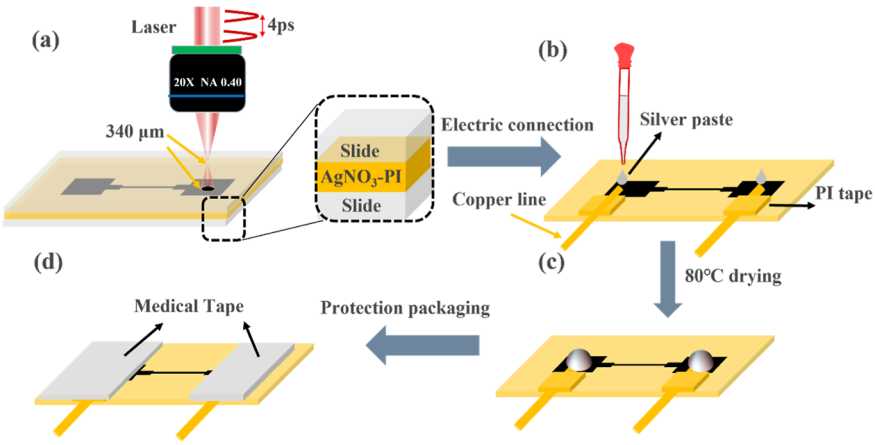

Figure 1. Schematic illustration of the fabrication process of the Ag-LIG bendable sensor: (a) patterning of the sensing unit, (b) electric connection of the sensing unit, (c) drying of the silver pastes, and (d) protection packaging of the sensing unit.

process. You et al. fabricated a noble metal nanoparticle−three-dimensional (3D) graphene-based immunosensor for the detection of *Escherichia coli* O157:H7 by using the one-step laser induction method.[21] Tien et al. adopted silver nanoparticles (Ag NPs) to improve the electrical conductivity of graphene nanosheets (GNS)−Ag composites with a minimum sheet resistance of 94 Ω/□.[22] Rahimi et al. prepared Ag−C composites by drying silver ink on LIG lines, and the sheet resistance decreased from 50 to 0.02 Ω/□.[12] Atli et al. utilized Pd, Ni, and Cu nanoparticles to realize polymer metallization.[23] Additionally, plasma confinement was applied to enhance the carbonization degree of the ablation zone with higher temperature and pressure.[24]

In this study, combining the temporal shaping, plasma ejection confinement, and silver nitrate doping, a Ag−C composite structure with a lateral resolution of 6.5 μm was fabricated by fs laser one-step direct writing for the first time, which was about 54% the reported high-resolution result of 12 μm.[24] The structure was further applied for the bending sensor. The sensitivity was optimized through controlling the conductivity and the line width of the sensing unit via tuning the laser fluence and the interpulse delay of the fs double pulses. A $\Delta R/R$ of ∼25.8% is demonstrated in cyclic bending and shows a quick and stable response to human pulse and finger bending.

2. EXPERIMENTAL SECTION

2.1. Materials. Poly(pyromellitic dianhydride-*co*-4,4′-oxydianiline), amic acid solution, 15.0−16.0 wt % in 1-methyl-2-pyrrolidinone (NMP), (PAA solution) was purchased from Sigma-Aldrich (St. Louis, Missouri, USA). Silver nitrate ($AgNO_3$) was obtained from Acros Organics, Fisher Scientific Worldwide Co., Ltd. (Shanghai, China). NMP, AR (>99%), was purchased from Innochem (Gyeonggi-do, South Korea). Fused quartz microscope slides (75 × 25 × 1 mm) were purchased from Hefei Kejing Materials Tech Co., Ltd. (Hefei, China).

2.2. Preparation of the Ag−PI Film. Briefly, 66.6 mg (2 wt %) and 100 mg (3 wt %) of silver nitrate powder were fully dissolved in 5 mL of NMP. The above solutions were then mixed with 22.22 g of PAA solution and stirred in a low-humidity area. The mixed solution was placed into a vacuum chamber for degassing. The suspension was poured into a glass mold, and the as-cast films were progressively dried in a muffle furnace at 80 °C for 1 h, 100 °C for 1 h, 200 °C for 1 h, 300 °C for 1 h, and 330 °C for 1 h. After imidization, the $AgNO_3$−PI film was peeled off the mold and cut into specimens of the same size for laser fabrication.

2.3. Preparation of the Ag-LIG Mechanical Sensor. First, the prepared $AgNO_3$−PI film was placed between two microscope slides for plasma confinement and then inscribed by the laser with a proper defocus distance (approximately 340 μm), as shown in Figure 1a. After the fabrication, the sensing unit was electrically connected to a copper wire by silver paste. To prevent the disconnection of the copper wire during the measurement and protect the connection spot while the silver pastes dried, a heat-resistant PI tape was used, as shown in Figure 1b. Then, the silver ink was dried at 80 °C for 30 min, as shown in Figure 1c. Finally, the connection spot of the copper wire was covered by medical tape to provide protection during the bending test, as shown in Figure 1d.

2.4. Electromechanical Characterization. The fluence and time delay dependence of the resistance were tested in a 2000 μm × 2000 μm laser-fabricated area using a two-probe method and a digital multimeter (34465A, Agilent, USA), as shown in Figure S1a. The sensor was fixed on the middle of two collinear motorized linear translation stages (CXPF50-80100, Zolic Instruments Co., Ltd. China) for the bending test, as displayed in Figure S1b. The gap between the stages is approximately equal to the total length of the sensing unit, and the detail of the sensor is shown in Figure S1c. During the bending testing, two testing wires were used to connect the electrodes of the sensor and the digital multimeter. The sampling time of the digital multimeter is set to be 1 ms. By using the software (Path Benchvue digital multimeter), the resistance changes of the sensor can be recorded. To realize the cyclic bending of the sensor, one of the stages was fixed, while the other was programed to move forward four times with a step of 500 μm and then backward 2000 μm.

2.5. Apparatus. The morphologies and energy-dispersive spectroscopy (EDS) spectra of the prepared samples were obtained using a field-emission scanning electron microscope (Hitachi SU8220) operated at an accelerating voltage of 10 kV. The Raman spectra were collected using a Raman spectrometer (Renishaw-inVia-Reflex) excited by a 532 nm laser with an exposure time of 10 ms. X-ray photoelectron spectroscopy (XPS) measurements (PHI Quantera) were obtained using a monochromatic Al Kα source (1486.6 eV).

https://doi.org/10.1021/acsomega.2c05060
ACS Omega 2022, 7, 42256−42263

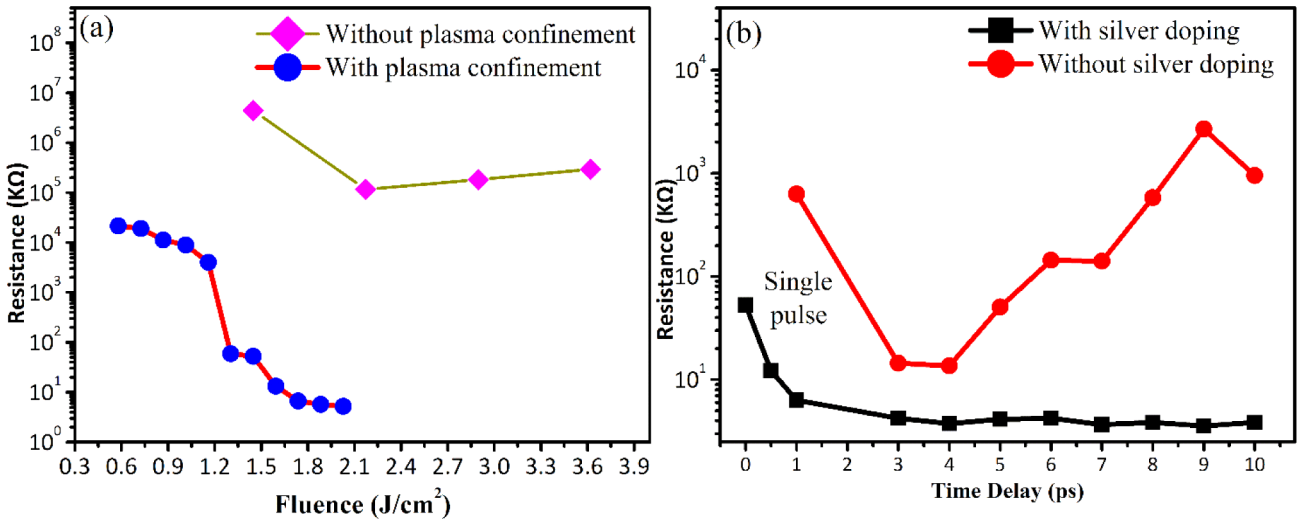

Figure 2. Resistance of the laser-treated PI film: (a) resistance of the laser-treated $AgNO_3$–PI film as the fluence ranged from 0.29 to 3.62 J/cm^2 and (b) resistance of the double pulse-treated PI film with a time delay in the range from 0 to 10 ps when the fluence was 1.45 J/cm^2 and $AgNO_3$ was doped in the PI precursor. The scanning speed and step were 2000 μm/s and 4 μm, respectively.

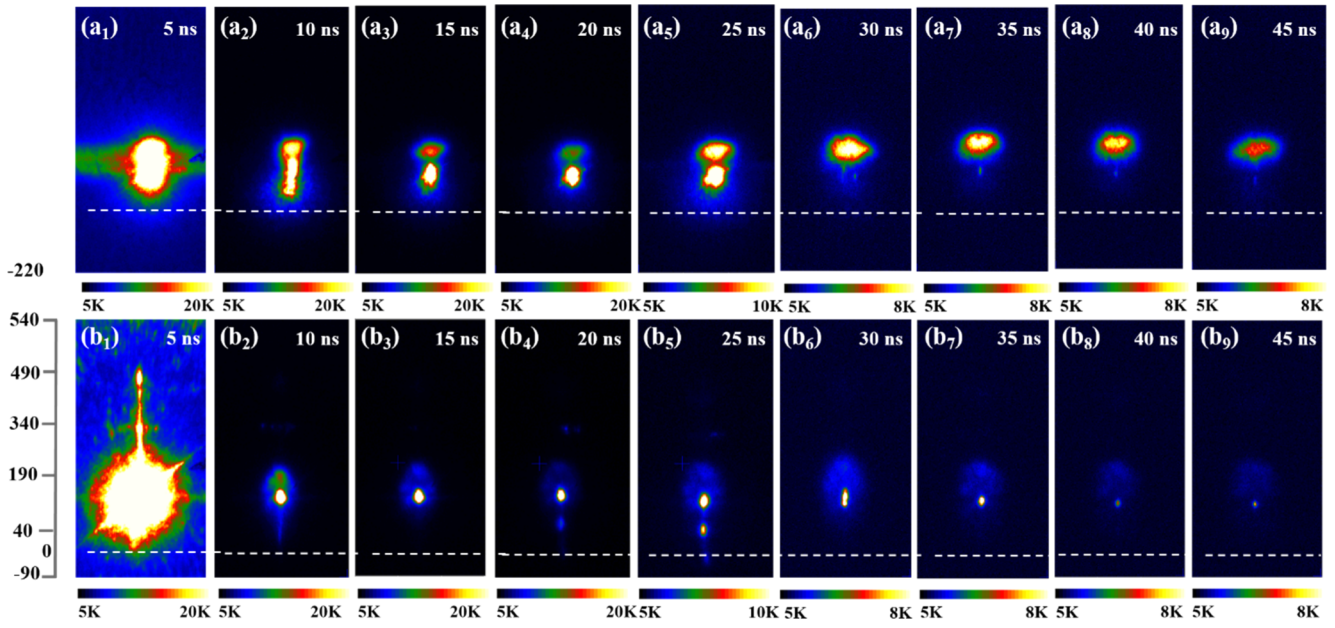

Figure 3. Time-resolved images of the laser-induced plasma plume of the Ag-doped PI film with a fluence of 1.45 J/cm^2: (a1–a9). without a slide cover and (b1–b9) with a slide cover.

The spatial resolution and energy resolution were 100 μm and <0.48 eV (Ag $3d_{5/2}$ full width at half maximum (FHWM)), respectively. Transmission electron microscopy (TEM) (JEM-2100) images of the Ag-NPs were observed at an acceleration voltage of 80 kV. For the TEM test, the samples were first scraped from a 5000 μm × 5000 μm laser-treated area and then immersed in 5 mL of ethanol solution for 30 min of sonication.

2.6. Experimental Setups. The fabrication and observation system contained a fs laser (Spitfire Pro-35F1KXP, wavelength: 800 nm, repetition rate: 1000 Hz, and pulse width: 35 fs), a six-axis stage (Physik Instrumente M-840.5DG) controlled by a computer, a charge-coupled device (CCD) camera, and an intensified CCD (ICCD, Andor iStar DH320T). The ICCD was used to obtain plasma images during laser fabrication. A Michelson interferometer was applied to generate double pulses with a tunable pulse delay. Other optics were used to control the beam direction and incident fluence. Details of the experimental setup are shown in Figure S2.

3. RESULTS AND DISCUSSION

3.1. Electrical Conductivity Enhancement. When a relatively lower laser fluence (below 1.45 J/cm^2) was used, it was difficult to form a continuous conductive pattern. With a higher fluence (above 1.45 J/cm^2) and an appropriate scanning interval, the fabricated area was covered by black amorphous carbon and became conductive. However, the resistance of the area that was laser-treated at different scanning speeds and scanning intervals remained on the order of megaohms, as shown in Figure S3. To further increase the conductivity, plasma confinement, temporal shaping, and silver doping were

https://doi.org/10.1021/acsomega.2c05060
ACS Omega 2022, 7, 42256–42263

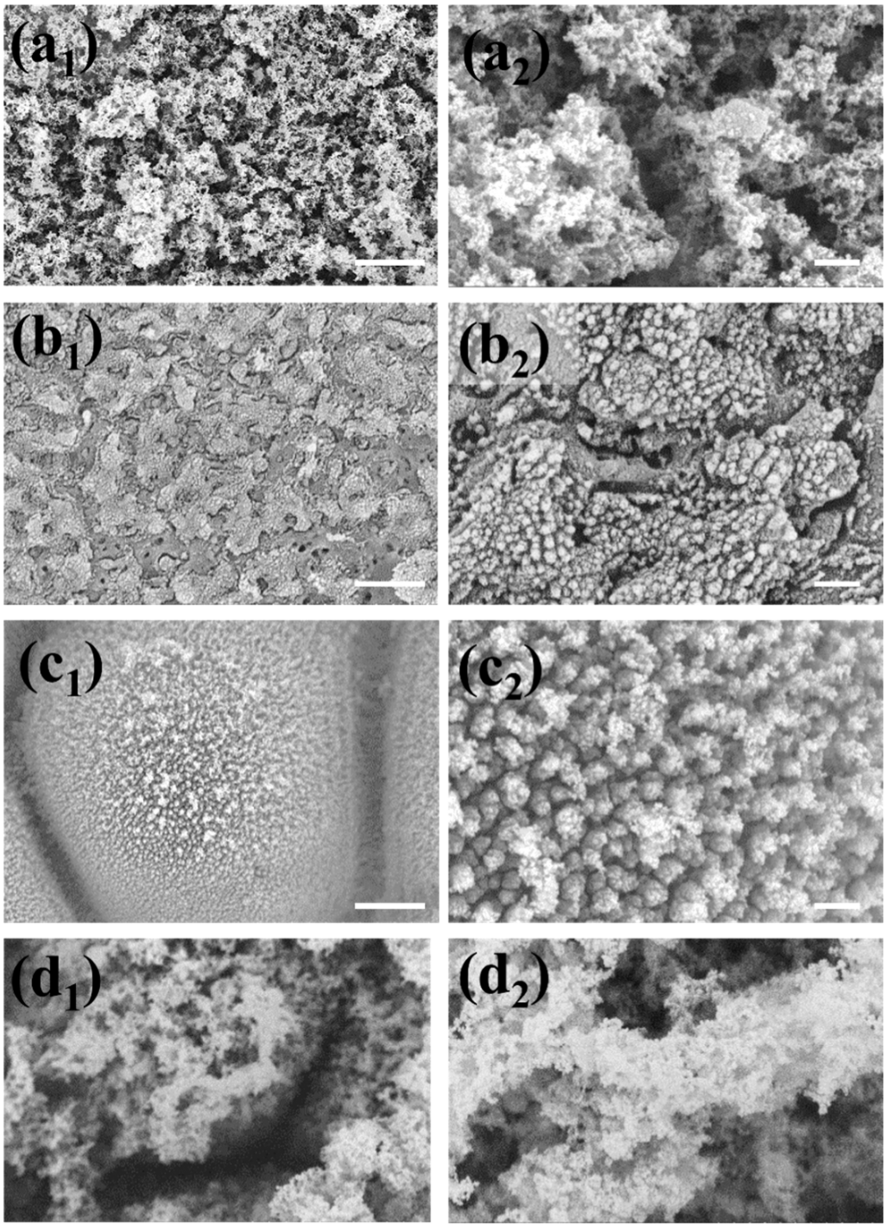

Figure 4. Morphology of the area laser-treated with different powers: (a1) 0.72, (b1) 1.45, and (c1) 2.17 J/cm^2 with double pulses of 4 ps delay and (d1) 1.45 J/cm^2 with single pulse. (a2−d2) Details of (a1−d1) with a scale bar of 200 nm. The scale bar in (a1−d1) is 2 μm.

applied, and the corresponding conductivity enhancement is shown in Figure 2.

To confine the debris generated during laser ablation and thus increase the conductivity, a slide cover was used over the $AgNO_3$-doped PI film. Figure 2a shows the dependence of the resistance on the laser fluence with or without a slide covering. The resistance of the laser ablation area without the slide covering is about hundreds of megaohms, which is higher than that with the slide covering. The relatively high resistance with a slide covering on the ablation zone indicates that plasma confinement is a feasible way to increase the conductivity. With the slide covering, the resistance of the carbonized $AgNO_3$-doped PI film changed from hundreds of megaohms to thousands of ohms. It began to decrease sharply as the fluence reached 1.02 J/cm^2 and finally became stable as the fluence reached 1.74 J/cm^2. The resistance reached its minimum at approximately 10 kΩ (0.001 Ω/□ with a sheet thickness of approximately 50 μm) when the fluence was 1.74 J/cm^2.

Silver nitrate, as a Ag NP precursor, was then added to the PAA solution before imidization. Moreover, double pulses with interpulse delays in the range of 0−10 ps were applied to stabilize the resistance. The resistance of the structure varied with the interpulse delay, as shown in Figure 2b. The minimum sheet resistance of the double pulse-treated area was approximately 0.0004 Ω/□ when the fluence was 1.45 J/cm^2, which is lower than the reported reference, as shown in Table S1. Notably, the difference in pulse energy distribution affected the instantaneous electron density and electron temperature[19] of excited $AgNO_3$-doped PI, further determining the intensity of the subsequent plasma emission, the ion kinetic energy, and the ion yield.[25] It was reported that the second pulse contributed to both crater formation and plasma reheating when the delay was in the range of 1−10 ps.[26] The

https://doi.org/10.1021/acsomega.2c05060
ACS Omega 2022, 7, 42256−42263

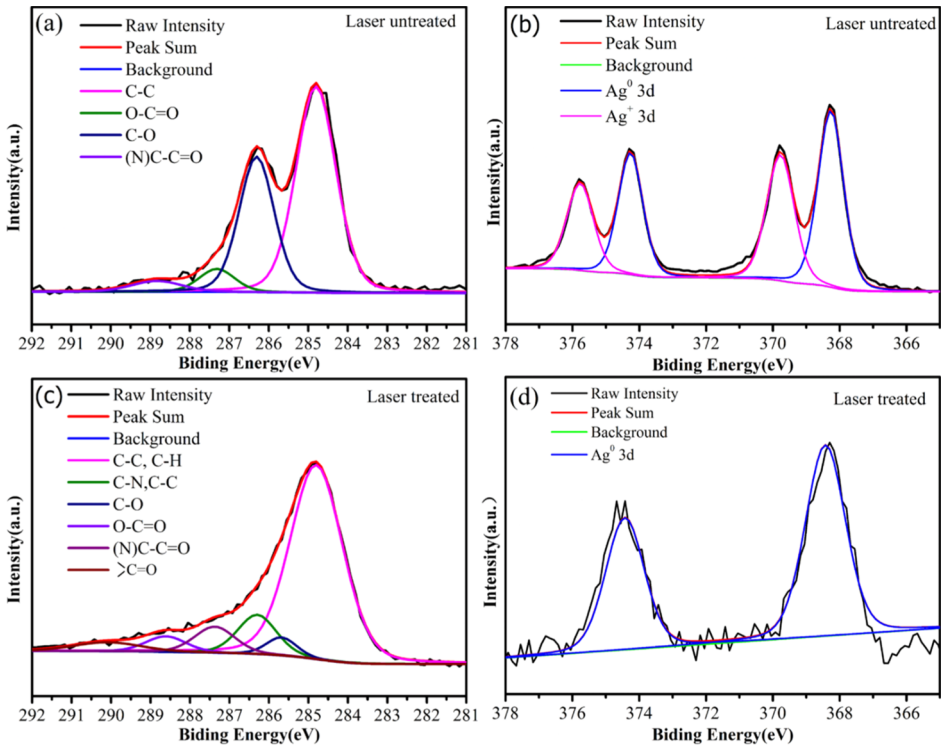

Figure 5. XPS spectra of the $AgNO_3$–PI films before and after laser fabrication when the fluence was 1.45 J/cm^2: (a) C 1s XPS spectrum before laser treatment; (b) Ag 3d XPS spectrum before laser treatment; (c) C 1s XPS spectrum after laser fabrication; and (d) Ag 3d XPS spectrum after laser fabrication.

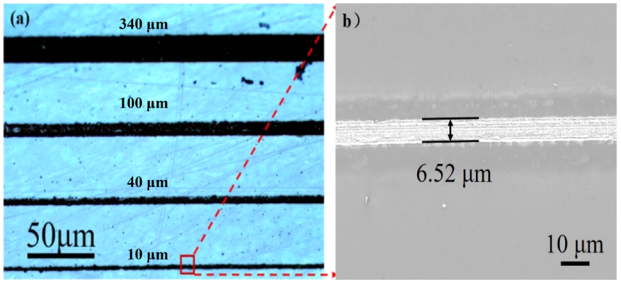

Figure 6. fs laser-induced Ag–carbon hybrid lines with different widths by defocusing at a fluence of 1.45 J/cm^2: (a) Ag–carbon hybrid lines with different widths by using different defocusing distances; and (b) detailed view of the Ag–carbon line when the defocusing distance is 10 μm.

decrease in resistance during the first 4 ps can be attributed to the increasing contribution of plasma reheating. With a further increase in the pulse delay, most of the energy of the second pulse was absorbed by the plasma induced by the first pulse, and the resistance showed good robustness for time delays of 4–10 ps. The resistance decreased from 52.7 kΩ for a single pulse (time delay of 0 ps) to approximately 4 kΩ for double pulses with a delay of over 4 ps.

By using the time-resolved images of the plasma emission after a single laser pulse (100 μJ), the ejection of plasma was observed. Figure 3(a1–a9) shows the laser-induced plasma plume images from 5 to 45 ns for the Ag-doped PI film without the slide cover. In the first 5 ns, only a slow plume component with high intensity was observed, as seen in Figure 3(a1). Similar to the form of plume emission of fused silica shown in ref 26, both slow and fast plume components were clearly observed, as shown in Figure 3(a2–a5). The plasma plume was ejected out the sample surface (white line) from 30 to 45 ns, as shown in Figure 3(a6–a9). With the slide covering, the plasma plume was more intense during the first 5 ns, as shown in Figure 3(b1). However, the intensity decreased quickly within 10 ns, as shown in Figure 3(b2–b5). Moreover, plume emission was barely visible after 30 ns, as shown in Figure 3(b6–b9). The plasma ejection was timely and spatially restricted within a relatively short time and limited space when using a slide covering. When multiple pulses were used, the energy- and laser-induced debris of the previous pulses was localized in a small zone. Thus, carbonization of PI and Ag ion reduction were more effective, which led to much lower resistance.

3.2. Structural Characterization. The conductivity enhancement has a strong relationship with the formation and melting of the porous conductive surface. Typical scanning electron microscopy (SEM) images of the fabricated structures are provided in Figure 4. When double pulses with an interpulse delay of 4 ps were applied (Figure 4a–c), at the fluence of 0.72 J/cm^2, the release of gases such as CO_2 or NO_2 during the ablation of PI converted the surface into porous structures, which are shown in Figure 4(a1,a2). The formation of this porous structure was accompanied by a decrease in resistance, as shown in Figure 2a. A higher fluence of 1.16 J/cm^2 generated enough heat to melt the porous structure into a surface deposited with homogeneous nanoparticles (Figure 4(b1,b2)), and the resistance became stable. When the fluence exceeded 1.74 J/cm^2, the nanoparticles finally melted and formed many bigger islands, as shown in Figure 4(c1,c2). Considering the thickness of the prepared film, a fluence above 2.17 J/cm^2 was not adopted because drilling occurred. Continuous deposition could not be obtained by the single pulse at the fluence of 1.45 J/cm^2, as shown in Figure

https://doi.org/10.1021/acsomega.2c05060
ACS Omega 2022, 7, 42256–42263

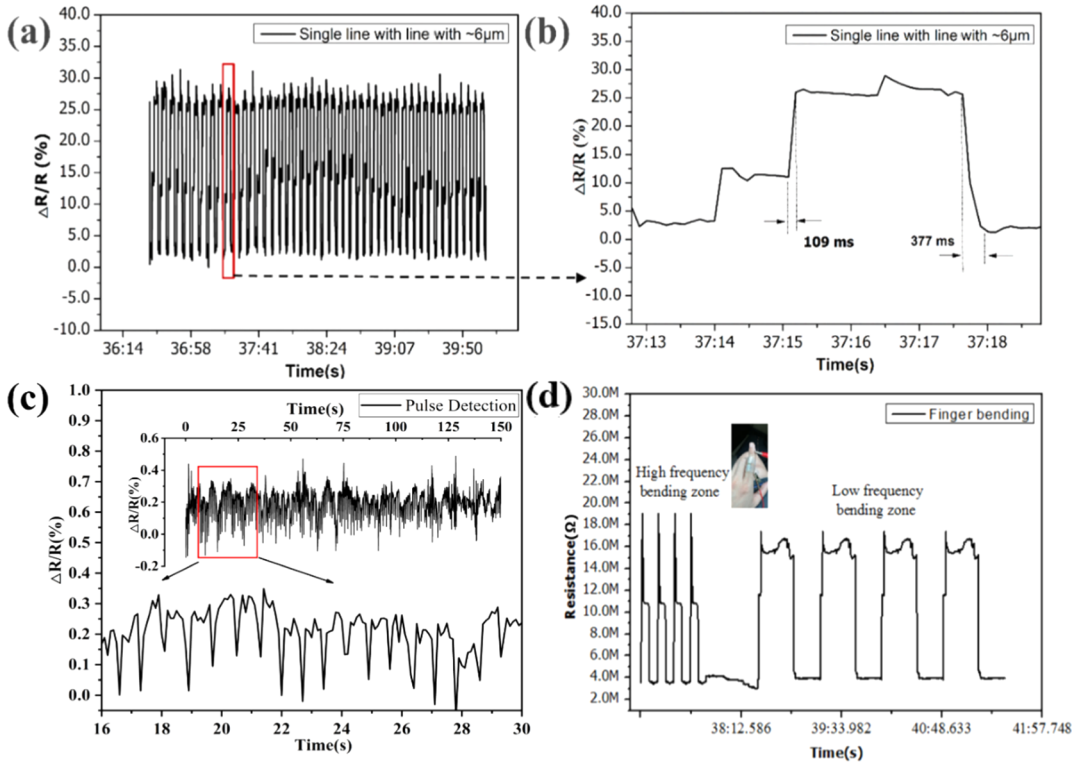

Figure 7. Bending test of the sensor with a line width of 6.5 μm and a length of 2000 μm: (a) cyclic bending test of the sensor; (b) response time of the sensor; (c) pulse detection; and (d) finger bending test results of the sensor.

4(d1,d2). The detailed evolution of the morphology as the fluence increased from 0.15 to 2.17 J/cm^2 can be found in Figure S5. The surface of the structure was covered by silver or silver oxide according to EDS mapping (Figure S4). Notably, similar morphologies were obtained after double-pulse fabrication with different interpulse delays, as shown in Figure S6. Combined with Figure 2b, we considered that the discontinuous distribution of the structure determined the conductivity.

To investigate the imidization of PAA, Fourier transform infrared (FTIR) spectroscopy was used. The presence of the characteristic peaks at 1717 cm^{-1} (imide C═O asymmetrical vibration) and 1778 cm^{-1} (imide C═O symmetrical vibration)[27] proved the successful imidization of PAA (Figure S7a) and the small effect of the doping of silver nitrate with respect to the weight ratio (Figure S7b). The laser-treated area, with or without plasma confinement, was also characterized by Raman spectra, as displayed in Figure S8. Clearly, two-dimensional (2D) peaks at 2697 cm^{-114} of the Raman spectra were not observed when plasma confinement was not applied, as shown in Figure S8a. However, the low intensity of the 2D peak shown in Figure S8b proved the presence of graphene. Compared with the 2D peak reported in the reference,[28] the low intensity was attributed to the relatively low heat effect when using a low repetition rate fs laser. The Ag−carbon hybrid structure was also observed by TEM images (Figure S9). Homogeneous deposition of silver NPs (see Figure S9a) and the *d*-spacing of wrinkled structures (3.42 Å see in Figure S9b) demonstrated the successful doping of silver and partial transformation from PI to graphene. Also, the *d*-spacing of nanoparticles shown in Figure S9c,d was 2.45 Å and close to the value corresponding to Ag(111) (JCPDS no. 89-3722), which suggests the Ag(111) facet on the surface of the Ag NPs.

To further validate the valence state of the laser-treated $AgNO_3$−PI film, XPS spectra were also measured. The spectra were fitted using Voigt line shapes with a mixing ratio *M* of 0.2 (*M* = 1.0 represents a pure Lorentzian function); additionally, a Tougaard-type inelastic background was used.[29,30] XPS Peakfit software was applied.[31] The full-range spectra shown in Figure S10 prove the presence of C, O, Au, and Ag before and after direct laser writing. Notably, the strong Au peaks were attributed to the Au coating during SEM testing. The fitting of the C 1s spectra is shown in Figure 5a,c. The spectrum was deconvoluted into six components with binding energy (BE) values of 284.8 eV (C−C bond of two benzene rings of the octadecylamine structure), 285.7 eV (C−C bond of the benzene ring in the pyromellitic dianhydride structure and the C−N bond), 286.3 eV (C−O bond), 287.4 eV (O−C═O bond), 288.6 eV [(N)C−C═O bond], and 290.2 eV (C═O).[32,33] The C−O peaks (286.3 eV) decreased after fabrication by the laser, indicating the carbonization of PI. As seen in Figure 5b,d, 368.3 eV (Ag^0 $3d_{3/2}$), 367.4 eV (AgO), 367.7 eV (Ag_2O), and 369.8 eV (bonded to organic PAA) were considered when fitting the Ag 3d spectra. Obviously, four spin−orbital splitting photoelectrons can be observed in Figure 5b which means that both silver oxide and silver are included in the $AgNO_3$−PI films. However, the decreasing number of orbital splitting peaks after laser fabrication shown in Figure 5d proves that the silver ions has been reduced to Ag NPs since the BE observed at 368.3 eV can be assigned to the Ag^0 $3d_{3/2}$.

3.3. High-Resolution Fabrication and Smart Sensing.

By changing the defocus distance of the laser beam, Ag-LIG specimens with different line widths were fabricated with a minimum line width of 6.5 μm, as shown in Figure 6.

https://doi.org/10.1021/acsomega.2c05060
ACS Omega 2022, 7, 42256−42263

The bend sensing capability of the produced Ag−carbon hybrid line was also evaluated by the experimental setup presented in Figure S2. The sensor with a line width of 6.5 μm was used for pulse detection and cyclic bending, as shown in Figure 7. By moving forward four times at a step of 500 μm and then backward 2000 μm to realize cyclic bending, the resistance variation (ΔR) divided by the resistance at the start of the measurement (R) was calculated to be ∼25.8%, as shown in Figure 7a. The tested sensor shows three distinct resistance changes at first threes 500 μm and displays a relatively rapid response time with its rising edge of 109 ms and falling edge of 377 ms, as shown in Figure 7b. The comparison of the strain sensor with the reported references are shown in Table S2. By mounting the sensor tightly on the wrist, the small strain of human body was detected. At least 18 peaks can be fully recognized during 16−30 s, as shown in Figure 7c, which indicates the potential of the sensor in human health monitoring. The sensor was also applied in finger-bending recognition when huge strains were applied. Figure 7d demonstrates good responses to finger motion with different frequencies.

4. CONCLUSIONS

In summary, the high-resolution Ag−carbon hybrid structures were fabricated by fs laser one-step direct writing. Combined with $AgNO_3$ doping and plasma confinement, a resolution of 6.5 μm was demonstrated with good conductivity. The sheet resistance was decreased to 0.0004 Ω/□. The thin line was applied as the bending sensor and showed good responses in human pulse and finger bending sensing.

■ ASSOCIATED CONTENT

Supporting Information

The Supporting Information is available free of charge at https://pubs.acs.org/doi/10.1021/acsomega.2c05060.

The experimental setup of the electromechanical test, the experimental setup of the laser system, the conductivity of the laser fabricated area without plasma confinement at different powers and scanning speeds when the scanning interval is 4 μm, EDS mapping of the structure with different fluences; the evolution of the morphology as the fluence is increased from 0.15 to 2.17 J/cm^2, the morphology of the temporally shaped laser-treated area with different time delays when the fluence is 1.45 J/cm^2, FTIR spectra of the $AgNO_3$−PI films, Raman spectra of a $AgNO_3$−PI film when the fluence is 1.45 J/cm^2, TEM images of the Ag-LIG flakes, and full-range XPS spectra of a $AgNO_3$−PI film before and after laser fabrication when the fluence is 1.45 J/cm^2 (PDF).

■ AUTHOR INFORMATION

Corresponding Author

Sumei Wang − *Laser Micro/Nano-Fabrication Laboratory, School of Mechanical Engineering, Beijing Institute of Technology, Beijing 100081, P. R. China; Yangtze Delta Region Academy of Beijing Institute of Technology, Jiaxing 314019, China;* orcid.org/0000-0002-5511-1344; Email: wangsumei@bit.edu.cn

Authors

Quan Hong − *Laser Micro/Nano-Fabrication Laboratory, School of Mechanical Engineering, Beijing Institute of Technology, Beijing 100081, P. R. China*

Weihua Zhu − *Laser Micro/Nano-Fabrication Laboratory, School of Mechanical Engineering, Beijing Institute of Technology, Beijing 100081, P. R. China*

Lan Jiang − *Laser Micro/Nano-Fabrication Laboratory, School of Mechanical Engineering, Beijing Institute of Technology, Beijing 100081, P. R. China; Beijing Institute of Technology Chongqing Innovation Center, Chongqing 401120, China;* orcid.org/0000-0003-0488-1987

Jiahua He − *Laser Micro/Nano-Fabrication Laboratory, School of Mechanical Engineering, Beijing Institute of Technology, Beijing 100081, P. R. China*

Jie Zhan − *Laser Micro/Nano-Fabrication Laboratory, School of Mechanical Engineering, Beijing Institute of Technology, Beijing 100081, P. R. China*

Xin Li − *Laser Micro/Nano-Fabrication Laboratory, School of Mechanical Engineering, Beijing Institute of Technology, Beijing 100081, P. R. China; Beijing Institute of Technology Chongqing Innovation Center, Chongqing 401120, China;* orcid.org/0000-0002-4743-5509

Xiaoming Zhao − *Tianjin Navigation Instruments Research Institute, Tianjin 300131, China*

Bingquan Zhao − *Tianjin Navigation Instruments Research Institute, Tianjin 300131, China*

Complete contact information is available at: https://pubs.acs.org/10.1021/acsomega.2c05060

Author Contributions

L.J., S.W., and Q.H. initiated the project and wrote the manuscript. Q.H. and W.Z. conducted laser processing and characterization. S.W. supervised and supported the work. J.Z., J.H., X.L., X.Z., and B.Z. made intellectual contributions and edited the manuscript.

Notes

The authors declare no competing financial interest.

■ ACKNOWLEDGMENTS

The work was financially supported by the Joint Funds of the National Natural Science Foundation of China (grant no. U2037205).

■ REFERENCES

(1) Ye, R.; James, D. K.; Tour, J. M. Laser-Induced Graphene: From Discovery to Translation. *Adv. Mater.* **2019**, *31*, 1803621.

(2) Wang, Y.; Wang, Y.; Zhang, P.; Liu, F.; Luo, S. Laser-Induced Freestanding Graphene Papers: A New Route of Scalable Fabrication with Tunable Morphologies and Properties for Multifunctional Devices and Structures. *Small* **2018**, *14*, 1802350.

(3) Hong, J.; Wu, J.; Mao, Y.; Shi, Q.; Xia, J.; Lei, W. Transferred Laser-Scribed Graphene-Based Durable and Permeable Strain Sensor. *Adv. Mater. Interfaces* **2021**, *8*, 2100625.

(4) Lv, P.; Li, X.; Zhang, Z.; Nie, B.; Wu, Y.-L.; Tian, H.; Ren, T.-L.; Wang, G. Z. Ultrathin encapsulated rGO strain sensor for gesture recognition. *Microelectron. Eng.* **2022**, *259*, 111779.

(5) Luo, S.; Hoang, P. T.; Liu, T. Direct laser writing for creating porous graphitic structures and their use for flexible and highly sensitive sensor and sensor arrays. *Carbon* **2016**, *96*, 522−531.

(6) Tao, L. Q.; Tian, H.; Liu, Y.; Ju, Z. Y.; Pang, Y.; Chen, Y. Q.; Wang, D. Y.; Tian, X. G.; Yan, J. C.; Deng, N. Q.; et al. An intelligent artificial throat with sound-sensing ability based on laser induced graphene. *Nat. Commun.* **2017**, *8*, 14579.

(7) Duan, X.; Yao, Y.; Niu, M.; Luo, J.; Wang, R.; Liu, T. Direct Laser Writing of Functional Strain Sensors in Polyimide Tubes. *ACS Appl. Polym. Mater.* **2019**, *1*, 2914−2923.
(8) Yang, Y.; Song, Y.; Bo, X.; Min, J.; Pak, O. S.; Zhu, L.; Wang, M.; Tu, J.; Kogan, A.; Zhang, H.; et al. A laser-engraved wearable sensor for sensitive detection of uric acid and tyrosine in sweat. *Nat. Biotechnol.* **2020**, *38*, 217−224.
(9) Hui, X.; Xuan, X.; Kim, J.; Park, J. Y. A highly flexible and selective dopamine sensor based on Pt-Au nanoparticle-modified laser-induced graphene. *Electrochim. Acta* **2019**, *328*, 135066.
(10) Ge, L.; Hong, Q.; Li, H.; Liu, C.; Li, F. Direct-laser-writing of metal sulfide-graphene nanocomposite photoelectrode toward sensitive photoelectrochemical sensing. *Adv. Funct. Mater.* **2019**, *29*, 1904000.
(11) Li, H.; Xia, X.; Guo, C.; Ge, L.; Li, F. Laser-induced nano-bismuth decorated CdS−graphene hybrid for plasmon-enhanced photoelectrochemical analysis. *Chem. Commun.* **2020**, *56*, 13784−13787.
(12) Rahimi, R.; Ochoa, M.; Ziaie, B. Direct Laser Writing of Porous-Carbon/Silver Nanocomposite for Flexible Electronics. *ACS Appl. Mater. Interfaces* **2016**, *8*, 16907−16913.
(13) Zhang, Z.; Song, M.; Hao, J.; Wu, K.; Li, C.; Hu, C. Visible light laser-induced graphene from phenolic resin: A new approach for directly writing graphene-based electrochemical devices on various substrates. *Carbon* **2018**, *127*, 287−296.
(14) Stanford, M. G.; Yang, K.; Chyan, Y.; Kittrell, C.; Tour, J. M. Laser-Induced Graphene for Flexible and Embeddable Gas Sensors. *ACS Nano* **2019**, *13*, 3474−3482.
(15) Lin, J.; Peng, Z.; Liu, Y.; Ruiz-Zepeda, F.; Tour, J. M. Laser-induced porous graphene films from commercial polymers. *Nat. Commun.* **2014**, *5*, 5714.
(16) Kulyk, B.; Silva, B. F. R.; Carvalho, A. F.; Silvestre, S.; Fernandes, A. J. S.; Martins, R.; Fortunato, E.; Costa, F. M. Laser-Induced Graphene from Paper for Mechanical Sensing. *ACS Appl. Mater. Interfaces* **2021**, *13*, 10210−10221.
(17) Carvalho, A. F.; Fernandes, A. J. S.; Leitão, C.; Deuermeier, J.; Marques, A. C.; Martins, R.; Fortunato, E.; Costa, F. M. Laser-Induced Graphene Strain Sensors Produced by Ultraviolet Irradiation of Polyimide. *Adv. Funct. Mater.* **2018**, *28*, 1805271.
(18) Stanford, M. G.; Zhang, C.; Fowlkes, J. D.; Hoffman, A.; Ivanov, I. N.; Rack, P. D.; Tour, J. M. High-Resolution Laser-Induced Graphene. Flexible Electronics beyond the Visible Limit. *ACS Appl. Mater. Interfaces* **2020**, *12*, 10902−10907.
(19) Jiang, L.; Wang, A. D.; Li, B.; Cui, T. H.; Lu, Y. F. Electrons dynamics control by shaping femtosecond laser pulses in micro/nanofabrication: modeling, method, measurement and application. *Light: Sci. Appl.* **2018**, *7*, 17134.
(20) Xu, C.; Jiang, L.; Li, X.; Li, C.; Shao, C.; Zuo, P.; Liang, M.; Qu, L.; Cui, T. Miniaturized high-performance metallic 1T-Phase MoS2 micro-supercapacitors fabricated by temporally shaped femtosecond pulses. *Nano Energy* **2020**, *67*, 104260.
(21) You, Z.; Qiu, Q.; Chen, H.; Feng, Y.; Wang, X.; Wang, Y.; Ying, Y. Laser-induced noble metal nanoparticle-graphene composites enabled flexible biosensor for pathogen detection. *Biosens. Bioelectron.* **2020**, *150*, 111896.
(22) Tien, H.-W.; Huang, Y.-L.; Yang, S.-Y.; Wang, J.-Y.; Ma, C.-C. M. The production of graphene nanosheets decorated with silver nanoparticles for use in transparent, conductive films. *Carbon* **2011**, *49*, 1550−1560.
(23) Atli, A.; Trouillet, V.; Cadete Santos Aires, F. J.; Ehret, E.; Lemaire, E.; Simon, S. A generalized sample preparation method by incorporation of metal−organic compounds into polymers for electroless metallization. *J. Appl. Polym. Sci.* **2021**, *138*, 50276.
(24) Zhang, C.; Yao, J.; Lan, S.; Trofimov, V. A.; Lysak, T. M. Effects of plasma confinement on the femtosecond laser ablation of silicon. *Opt. Commun.* **2013**, *308*, 54−63.
(25) Babushok, V. I.; DeLucia, F. C.; Gottfried, J. L.; Munson, C. A.; Miziolek, A. W. Double pulse laser ablation and plasma: Laser induced breakdown spectroscopy signal enhancement. *Spectrochim. Acta, Part B* **2006**, *61*, 999−1014.
(26) Semerok, A.; Dutouquet, C. Ultrashort double pulse laser ablation of metals. *Thin Solid Films* **2004**, *453−454*, 501−505.
(27) Diaham, S.; Locatelli, M. L.; Lebey, T.; Malec, D. Thermal imidization optimization of polyimide thin films using Fourier transform infrared spectroscopy and electrical measurements. *Thin Solid Films* **2011**, *519*, 1851−1856.
(28) Lin, J.; Peng, Z.; Liu, Y.; Ruiz-Zepeda, F.; Ye, R.; Samuel, E. L.; Yacaman, M. J.; Yakobson, B. I.; Tour, J. M. Laser-induced porous graphene films from commercial polymers. *Nat. Commun.* **2014**, *5*, 5714.
(29) Stobinski, L.; Lesiak, B.; Malolepszy, A.; Mazurkiewicz, M.; Mierzwa, B.; Zemek, J.; Jiricek, P.; Bieloshapka, I. Graphene oxide and reduced graphene oxide studied by the XRD, TEM and electron spectroscopy methods. *J. Electron Spectrosc. Relat. Phenom.* **2014**, *195*, 145−154.
(30) Major, G. H.; Fairley, N.; Sherwood, P. M.; Linford, M. R.; Terry, J.; Fernandez, V.; Artyushkova, K. Practical guide for curve fitting in X-ray photoelectron spectroscopy. *J. Vac. Sci. Technol., A* **2020**, *38*, 061203.
(31) Kwok, R. XPS Peak Fitting Program for WIN95/98 XPSPEAK Ver. 4.1. 2000, https://warwick.ac.uk/fac/sci/physics/research/condensedmatt/surface/exp/xps/links/xpspeak_manual.doc (accessed April 01, 2022).
(32) Ektessabi, A.; Hakamata, S. XPS study of ion beam modified polyimide films. *Thin Solid Films* **2000**, *377*, 621−625.
(33) Yung, K. C.; Zeng, D.; Yue, T. M. XPS investigation of Upilex-S polyimide ablated by 355 nm Nd: YAG laser irradiation. *Appl. Surf. Sci.* **2001**, *173*, 193−202.

https://doi.org/10.1021/acsomega.2c05060
ACS Omega 2022, 7, 42256−42263